

# Ultrasonic defect detection in a concrete slab assisted by physics-informed neural networks

Sangmin Lee <sup>a</sup> , John S. Popovics <sup>b,\*</sup>

<sup>a</sup> Los Alamos National Laboratory, Los Alamos, NM, 87545, USA

<sup>b</sup> Department of Civil and Environmental Engineering, University of Illinois at Urbana-Champaign, 205 North Mathews Avenue, Urbana, IL, 61801, USA

## ARTICLE INFO

### Keywords:

Concrete  
Defects  
Imaging  
Machine learning  
Neural networks  
Nondestructive testing  
PINNs  
Surface waves

## ABSTRACT

Traditional nondestructive testing (NDT) methods face challenges to accurately assess concrete owing to its naturally inhomogeneous nature that complicates spatial characterization of material properties. To address these limitations, this work considers physics-informed neural networks (PINNs) interpreting contactless ultrasonic scan data to enhance defect detection capabilities in concrete. PINNs integrate physics laws through mathematical governing equations into artificial neural network models to overcome limitations of purely data-driven analysis approaches. The study utilizes experimental data collected from a large-scale concrete slab containing inclusion, cold joints with cracks, and surface fire damage and from a homogeneous PMMA slab (as a reference). The PINN results are used to create space-dependent property maps based on the extracted coefficient of the governing wave equation using a simple time-domain wavefield data set. The results demonstrate that PINNs effectively predict space-dependent wave velocities. This approach facilitates accurate material property characterization and defect identification. The proposed PINN models achieved a P-wave velocity prediction error of 0.34 % for the PMMA slab and identified areal extent of defects in the concrete slab with errors of 1 % for pristine areas and 2.1 % for inclusion areas. Sub-wavelength-sized cracks around the inclusion areas were detected from the predicted wave velocity map. These findings suggest that PINNs offer a promising approach for improving the accuracy and efficiency of defect detection in concrete structures with superior spatial resolution provided by other conventional ultrasonic imaging approaches.

## 1. Introduction

The importance of nondestructive testing (NDT) methods and structural health monitoring techniques is increasingly recognized in the context of characterizing the aging built infrastructure in United States [1]. This is especially important now because the built infrastructure is subjected to more severe environmental changes owing to unusual weather events driven by climate change and global warming. Concrete is a ubiquitous material in the built infrastructure and establishing its condition is paramount for public safety. Therefore, researchers have made a great effort to develop effective assessment methods [2]. The most commonly used assessment are well documented in ACI 228.1R-03 [3] and ACI 228.2-R13 [4], which provide guidance on in-place concrete strength estimation methods and NDT methods for concrete condition evaluation, respectively. These methods can be divided into two main categories. The first category is invasive (or semi-destructive) methods such as Penetration resistance [5], pullout test [6], coring [7], etc.;

although, in most cases, a calibration curve is required to correlate the response from a method to material properties such as compressive strength; these methods are intuitive and relatively simple to perform. However, these methods require repair after testing, may degrade the quality of the structure, and may provide an opportunity for additional damage mechanisms to progress. The other category is nondestructive methods such as Schmidt hammer [8], impact-echo [9], ultrasonic pulse velocity (UPV) [10], ultrasonic-echo, radiography [11], infrared thermography [12], concrete resistivity [13], etc. Each of these methods has advantages and limitations, and an investigator should select an appropriate method and make a scientific plan.

One of the main challenges for concrete integrity assessment and defect detection is the inherent large-scale inhomogeneous nature of concrete, complicating the spatial characterization of its properties through traditional NDT methods that typically rely on point-to-point measurements that are limited in number and areal extant of coverage. In addition, conventional NDT methods often lack sensitivity

\* Corresponding author.

E-mail address: [johnpop@illinois.edu](mailto:johnpop@illinois.edu) (J.S. Popovics).



to subtle damage occurrences, necessitating robust solutions capable of comprehensive structural analysis. Contactless sensing methods present a promising alternative by overcoming the limitations inherent in conventional NDT methods. These methods, particularly contactless mechanical wave sensing, offer benefits such as freedom from mechanical sensor coupling issues (caused by devices like accelerometers or piezoelectric sensors), reduction in measurement time, and facile scanning of relatively large areas. Air-coupled transducers (ACT) in particular have been recently utilized for mechanical wave sensing. Although air-coupled sensors were developed several decades ago [14,15], research on NDT with ACT began in the 1980s [16–18] and gained momentum in the early 2000s [19,20]. In the field of civil engineering, significant research has been conducted over the last decade using contactless sensing methods. For example, contactless sensing methods have been used with the impact-echo method [19,21], concrete rail tie assessments [22], cracking damage evaluation [23–25], alkali-silica reaction damage detection [26], and early-age concrete monitoring [27]. Despite their potential and the ongoing research efforts, there is currently no standard for contactless sensing methods, and their application in the field remains limited. Further validation using real-world scenarios with the establishment of standardized protocols, coupled with improved signal processing techniques and the adoption of advanced machine learning algorithms that make use of the beneficial aspects of large data sets offered by air-coupled sensing, could significantly enhance their adoption and effectiveness in the field.

Machine learning technology has become increasingly prevalent, influencing not only academia and industry but also everyday individuals. Machine learning techniques, including artificial neural networks (ANNs), have been under development since the 1940s and 1950s [28]. Two periods represent significant milestones in the development and popularization of machine learning: the 1990s and the 2010s. In the 1990s, several notable neural network architectures were proposed, including Long Short-Term Memory (LSTM) [29] for speech recognition applications and convolutional neural networks (CNNs) [30] for image and video applications. In addition, Support Vector Machine (SVM) [31] was introduced, which is a supervised machine learning algorithm that classifies data by finding an optimal hyperplane to maximize the margin between different classes. Considering everyday applications, IBM's Deep Blue [32] defeated a human chess champion in 1997 – the first time a computer had beaten a world champion. The next significant surge in machine learning's popularity occurred in the 2010s, driven by the availability of vast amounts of data and significant increases in computing power, particularly GPUs. AlexNet, a deep CNN architecture, won the ImageNet Large Scale Visual Recognition Challenge (ILSVRC) [33], establishing CNNs as the mainstream in deep learning. The introduction of Generative Adversarial Networks (GANs) [34] marked a significant advancement in generative AI capabilities. Furthermore, the release of popular Python packages such as TensorFlow and PyTorch, in 2015 and 2016 respectively, facilitated the widespread adoption of deep learning models in industry, including applications like Google Photos and Waymo's self-driving systems.

Currently, most deep learning models rely purely on data-driven approaches. However, there are several limitations to purely data-driven approaches: (1) these models often operate as “black boxes”, offering little insight into their internal processes and decision-making mechanisms, which can hinder deeper understanding of how the model predicts results; (2) they require a tremendous amount of training data to learn targeted behaviors, which can be challenging to obtain and manage; (3) the high computational power required, particularly for training deep models, can be burdensome; and (4) they may exhibit poor performance on unseen data, leading to generalization errors or overfitting problems. In addition to these limitations, a major issue with data-driven approaches in engineering applications is that conventional data-driven models may yield physically inadmissible solutions owing to insufficient information about the governing laws of mechanics and physics that underlie the problem of interest. To mitigate these

problems, researchers have proposed the direct implementation of physical laws as prior knowledge into ANNs; this is known as physics-informed neural networks (PINNs). Although PINNs are a relatively new technique within the realm of machine learning and neural networks [35], the concept itself is not new [36,37]. PINNs incorporate physics-based equations, typically differential equations, as prior knowledge within the training and prediction process, unlike conventional ANNs that do not utilize prior knowledge or physical laws related to the prediction target. In conventional ANNs, parameters such as weights and biases are learned solely through training data.

This paper demonstrates a method for material characterization and defect detection in concrete using contactless ultrasonic scanning data processed using PINNs. The primary contribution of this study is the prediction of space-dependent material properties, facilitating defect detection, at higher spatial resolution than that offered by other imaging methods such as tomography, synthetic aperture focusing, and time-reversal analysis. A simple time-domain wavefield is used as input to predict the complete wave velocity map of the area of interest, where only 70 % of the total wavefield data are used for training, demonstrating the robustness of the proposed model. The results presented in this study are based on experimental data collected from a large-scale concrete slab, a primary structural component in the construction field, in contrast to most PINN-related studies that rely only on simulated data sets. To the best of the authors' knowledge, this study presents the first application of PINNs to large-scale concrete specimens for damage detection and prediction of space-dependent properties thereby providing images that enhance damage detection. The paper is structured as follows: First, the fundamental algorithms for PINNs are briefly reviewed, and the developed PINN models are introduced. Next, two test specimens are described: a PMMA slab (for reference purposes) and a large-scale concrete slab containing multiple types of defects. Following this, the experimental setups for both fully contactless and semi-contactless methods are described. The results section then evaluates the performance of the proposed PINN methods. Finally, the conclusions of the study are presented.

## 2. Physics-informed neural networks

The PINN architecture used in this study is based on fully-connected neural networks where the model is expressed mathematically as

$$\hat{u} = f_{\theta}(\mathbf{p}) \quad (1)$$

where  $\hat{u}$  are the output values from ANN which serve to predict true value of  $u$ ,  $f_{\theta}$  the ANN expressed as a function,  $\theta$  the learnable parameters (such as weights and biases in neurons), and  $\mathbf{p}$  the input data set. In this paper, the hat symbol ( $\hat{\cdot}$ ) represents a prediction. Fig. 1 shows the PINN architecture used in this study. The input layer accepts three variables which are two special coordinates ( $x, y$ ) and time ( $t$ ). Then, the input data undergo z-score normalization, which adjusts them to have a mean value of 0 and a standard deviation of 1. This practice is common to enhance the convergence speed of ANNs [38]. After that, the normalized data are passed into the fully-connected layer network, named the ‘Main network.’ The main network is used to predict output values (i.e., wave field, displacement, pressure) where the output values are expressed as  $\hat{u}$ . According to the universal approximation theorem [39,40], the output value can be considered as a continuous function where the value is differentiated with regard to the input data ( $x, y$ , and  $t$ ) using automatic differentiation [41,42]. The differentiated values (e.g.,  $\partial^2 \hat{u} / \partial t^2, \partial^2 \hat{u} / \partial x^2$ ) are multiplied with a predicted corresponding coefficient to calculate the residual ( $\mathcal{R}$ ) of the implemented physics-based equation. The coefficient here is the wave velocity,  $c_0$  that is predicted from the ‘subnetwork’. As shown in Fig. 1, the subnetwork is also a fully-connected layer and it accepts only spatial coordinates ( $x, y$ ) as input variables, so the wave velocity is a function of spatial variables and thus suitable for heterogeneous material characterization.

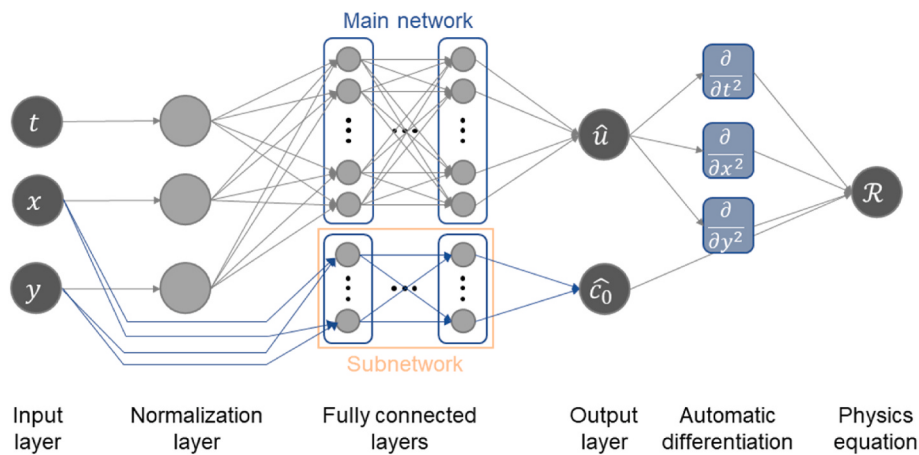


**Fig. 1.** PINN architecture used in this study: the coefficient ( $\hat{c}_0$ ) is calculated from the subnetwork. The subnetwork accept spatial coordinates to ensure that material properties vary over space.

In this study, a concrete slab is the target structure, which serves as a reasonable representative of an actual concrete structure. Because the wavelength of the ultrasound is sufficiently smaller than the thickness of the slab, a pure Rayleigh wave approximation of the measured wave propagation behavior is reasonable. We consider the material properties of the concrete in the slab to be homogeneous with respect to the depth (but not spatially), which is a commonly found scenario [43]. These assumptions allow us to represent the wave behavior using a simplified 2-D Rayleigh wave equation:

$$\frac{\partial^2 u}{\partial t^2} = c_0^2(x, y) \left( \frac{\partial^2 u}{\partial x^2} + \frac{\partial^2 u}{\partial y^2} \right). \quad (2)$$

The PINN architecture used here has one subnetwork because there is only one unknown coefficient in Eq. (2), which is the Rayleigh wave velocity. If the number of unknown coefficients in the corresponding governing equation is more than one, the number of subnetworks could also be expanded. The cost function for the PINN architecture used here is defined as

$$J(\theta) = \frac{\lambda_1}{N} \sum_{i=1}^N [f(\mathbf{p}_i) - \hat{f}_\theta(\mathbf{p}_i)]^2 + \frac{\lambda_2}{N} \sum_{i=1}^N [\mathcal{R}(\mathbf{p}_i)]^2 \quad (3)$$

where  $N$  is the total number of training data,  $\lambda_1, \lambda_2$  the weights used to balance between terms,  $f(\mathbf{p}_i)$  the latent true function or labeled output data, and  $\mathcal{R}(\mathbf{p}_i)$  the residual of physics-based equations. The form of  $\mathcal{R}(\mathbf{p}_i)$  depends on the application and the implemented governing equations. In this study the residual ( $\mathcal{R}$ ) is defined as

$$\mathcal{R}(\mathbf{p}_i) := \frac{\partial^2 \hat{f}_\theta(\mathbf{p}_i)}{\partial t^2} - \{ \hat{c}_0(x, y) \}^2 \left( \frac{\partial^2 \hat{f}_\theta(\mathbf{p}_i)}{\partial x^2} + \frac{\partial^2 \hat{f}_\theta(\mathbf{p}_i)}{\partial y^2} \right) \quad (4)$$

where  $\hat{c}_0(x, y)$  is the predicted space-dependent Rayleigh wave velocity. Unlike the data fitting term, no true value is needed to calculate the residual. In other words, the true output values of the main network ( $f(\mathbf{p}_i)$ ) are provided during the training process, but the true coefficient values are not. The coefficients are predicted during the training process by minimizing the residual term. In this study, a total of 3 hidden layers each with 240 neurons was used as the main network and a total of 3 hidden layers each with 40 neurons. The weights  $\lambda_1$  and  $\lambda_2$  in Eq. (3) are 1 and 100, respectively. The Adam optimizer was used to train both main network and subnetwork with initial learning rates of  $1e^{-4}$  and  $5e^{-4}$ , respectively. These learning rate values provided a balance of convergence speed and training stability in our neural network architecture. Higher learning rate values resulted in training instability and oscillatory behavior in the loss function, preventing proper convergence, while lower learning rate values led to significantly slower convergence

and increased computational costs without meaningful improvements in model performance. The total number of training epochs is 50,000. For the training of the PINN models, only 70 % of the total data was utilized. It is not reasonable to choose randomly 70 % of the data among the entire data set because, in practice, it is unusual to collect the data with different sampling intervals. Instead, 70 % of spatial coordinates were randomly selected and only data corresponding to these coordinates was used as the training data. All hyperparameters for the PINN models used in this study are summarized in Table 1.

### 3. Test specimens

Two slab specimens were used for experimental verification. One is a lab-scale PMMA slab which has homogeneous material properties. The other is a large-scale concrete slab containing cold joint and surface damage defects. A PMMA slab, selected for its homogeneous material properties, has dimensions of  $635 \times 610 \times 77$  mm. To the author's knowledge, the slab is free of defects. To verify PINN prediction results, reference wave velocity data were obtained using the conventional UPV method. Three measurements were performed: two through the thickness and one along the width of the specimen. Table 2 lists the P-wave velocities obtained from the UPV test. The average P-wave velocity from UPV measurements is 2747 m/s.

In addition to the PMMA slab, a large-scale concrete slab was prepared. The specimen was designed with two different concrete mixtures to simulate both a cold joint defect and section of poor-quality of concrete (soft inclusion). To place two different mixtures, an additional inner mold was made within the primary mold for the entire slab as shown in Fig. 2. The inclusion area was not cast simultaneously with the pristine area. Instead, four hours after casting the pristine area, the mold for the inclusion area was removed, and the inclusion mixture was cast as shown in Fig. 3 (a). This process led to the development of cracks along each corner when the inner mold for the inclusion area was removed, as shown in Fig. 3 (b). The w/c ratio for the pristine and inclusion areas were 0.45 and 0.75, respectively, with the latter intentionally elevated to represent inferior concrete quality. Both mixture designs incorporated 20 % replacement of cement with fly ash by weight, as detailed in Table 3. The coarse aggregate within the pristine and inclusion areas consisted of limestone chip and river gravel, respectively, both with a maximum aggregate size of 9.5 mm [3/8 in]. The slab, shown in Fig. 2, measures  $2 \text{ m} \times 1.5 \text{ m} \times 0.3 \text{ m}$ . A reference direction is defined and indicated by "N" and an arrow in the figure.

In order to establish material reference data, companion cylinders (Diameter = 101 mm [4 in], height = 203 mm [8 in]) were prepared from the same batch for the inclusion mixture (3 cylinders) and pristine mixture (4 cylinders), respectively. P-wave velocity was measured using

**Table 1**

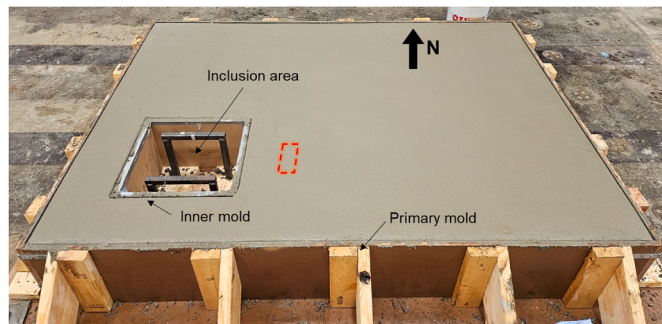
The hyperparameters of the PINN models.

Case	Main network		Subnetwork		Weights		Learning rate		Batch size	Epoch	Training data <sup>a</sup>
	Layer	Neurons	Layer	Neurons	$\lambda_1$	$\lambda_2$	Main network	Subnetwork			
PMMA slab	3	240	3	40	1	100	1.00E-04	5.00E-04	8192	5.00E+04	41009
Concrete slab – inclusion defect	3	240	3	40	1	100	1.00E-04	5.00E-04	8192	5.00E+04	96112
Concrete slab – surface damage	3	240	3	40	1	100	1.00E-04	5.00E-04	32768	5.00E+04	178385

<sup>a</sup> Training data represents a pair of  $(x, y, t)$  and  $u(x, y, t)$ .**Table 2**

UPV test results from the PMMA slab.

Measurement direction	P-wave velocity [m/s]
Through the length	2727
Through the thickness 1	2750
Through the thickness 2	2766
Mean	2747

**Fig. 2.** The large-scale concrete slab after casting the pristine portion. The inclusion area was cast four hours later and remained unfilled during the interim time.

the conventional through-thickness UPV method along the length of the cylinder. The 1<sup>st</sup> and 2<sup>nd</sup> longitudinal mode resonance frequencies of the cylinders were measured using the impact resonance method [44]. The resulting data are shown in Table 4. Typical Poisson's ratio values of concrete are expected to be between 0.1 and 0.25 [45,46]. A Poisson's ratio value of 0.2 is normally assumed when Poisson's ratio is not measured directly. However, rather than using a typical Poisson's ratio, Poisson's ratio were calculated using the 1<sup>st</sup> and 2<sup>nd</sup> longitudinal

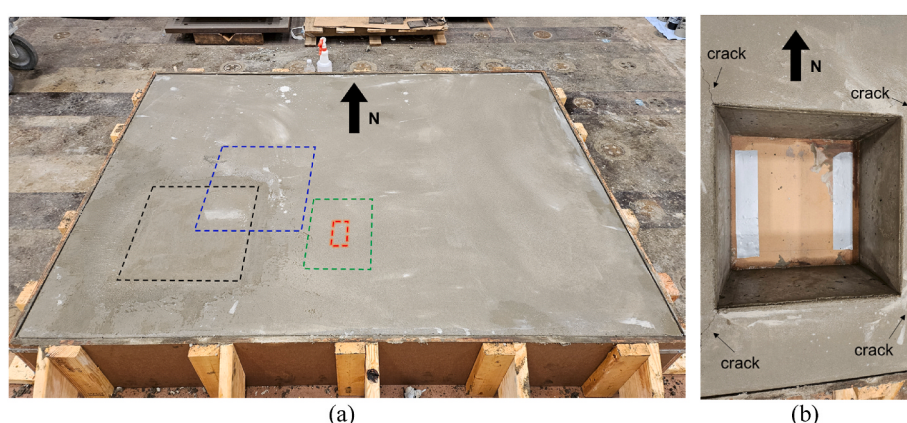
resonance frequencies [47]. Based on the UPV results, the mean value of the P-wave velocity for the pristine mix is 4168 m/s and that for the inclusion part mix is 3533 m/s.

In addition to the cold joint defect, local surface damage was implemented using a propane gas torch, where the location of the damaged region is indicated by the small red rectangle in Fig. 3 (a). A localized area of fire damage, measuring 87 × 40 mm, was created by first placing steel plates on the slab's surface, as shown in Fig. 4 (a). These plates ensured that only the targeted area of the concrete surface was exposed to direct flame. The fire damage process was repeated five times, with each instance lasting for 30 s with a 3 to 5-min interval between each flame exposure period to prevent overheating of the specimen. The primary objective of this damage mechanism was to induce microcracking caused by moisture loss, rather than to cause a phase change in the aggregate. Fig. 4 (b) presents the surface temperatures captured by an infrared camera immediately after one of the flame exposure damage processes. A phase change in the aggregate is not expected because the maximum surface temperature is below 130 °C. Fig. 5 show detailed images of one area where the flame surface damage was applied. No visible cracks are seen before the flame exposure process. However, after the flame exposure damage process, microscale cracks appeared in the cement matrix and around the aggregate, as shown in Fig. 5 (b).

**Table 3**

Two different concrete mixture designs used for the large-scale concrete slab.

Material	Amount (kg/m <sup>3</sup> [lb/yd <sup>3</sup> ])	
	Inclusion	Pristine
Water	181 [305]	163 [275]
Cement	193 [325]	290 [489]
Fly ash	48 [81]	72 [122]
Coarse aggregate	722 [1217]	807 [1360]
Fine aggregate	1088 [1834]	1054 [1777]

**Fig. 3.** The concrete slab specimen after complete casting: (a) top view of the slab specimen and (b) a detailed view of the inclusion area before casting. The black dashed square in (a) indicates the inclusion area, the red dashed square indicates the fire-damaged area, and the blue and green dashed rectangles indicate scanning areas to detect the cold joint defect and the surface damage regions, respectively. During the process of inner mold removal, cracks developed at each corner, as indicated in (b). (For interpretation of the references to color in this figure legend, the reader is referred to the Web version of this article.)

**Table 4**

Test results obtained from companion cylinder samples for the concrete comprising the slab.

Cylinder samples	Resonance frequency [Hz]		Poisson's ratio ( $\nu$ )		UPV [m/s]	
	1 <sup>st</sup> mode	2 <sup>nd</sup> mode	Individual	Mean	Individual	Mean
Inclusion 1	8025	15457	0.183	0.18	3539	3533
Inclusion 2	8045	15505	0.181		3554	
Inclusion 3	7854	15194	0.167		3507	
Pristine 1	9481	18261	0.183	0.18	4177	4168
Pristine 2	9526	18356	0.181		4191	
Pristine 3	9347	18067	0.170		4129	
Pristine 4	9539	18340	0.189		4174	

#### 4. Experimental setup

Two different test configurations were used for the PMMA slab and the concrete slab, respectively. The test configuration for the PMMA slab is shown in Fig. 6 (a) where a fully contactless ultrasound measurement system was used. An ACT with a center frequency of 42 kHz (NCG50-D50 from Ultran Group) was used to generate Rayleigh waves. Although this study technically measures leaky Rayleigh waves propagating across an air-solid interface, the velocity difference between leaky Rayleigh waves and Rayleigh waves is negligible [48–50]. Therefore, the measured waves are treated as true Rayleigh waves in the following analysis. To collect wave propagation data over area of interest, a broadband ACT (BAT-1, Microacoustic Instruments Inc.) was used. The incident wave angle from the transmitter was adjusted to have 14–15°

considering that the 2nd critical angle is 14.9° ( $\sin^{-1} \left( \frac{340[m/s]}{1316[m/s]} \right)$ ). In

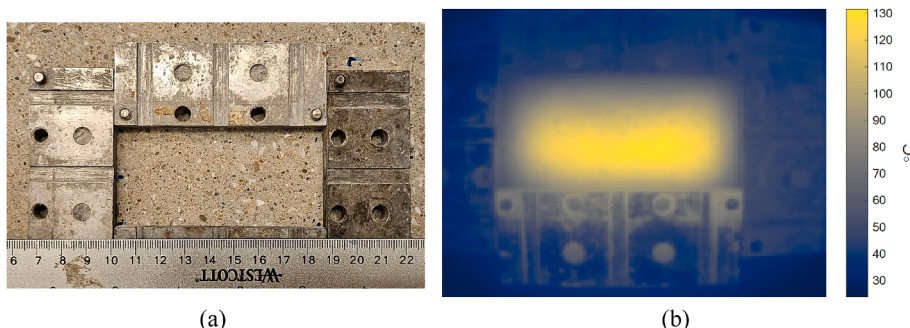


**Fig. 4.** Fire damage area: (a) a detailed view of the local surface damage area and (b) an infrared image taken after 5–10 s of the fire damage process. A temperature gradient is observed, with the maximum surface temperature not exceeding 130 °C.

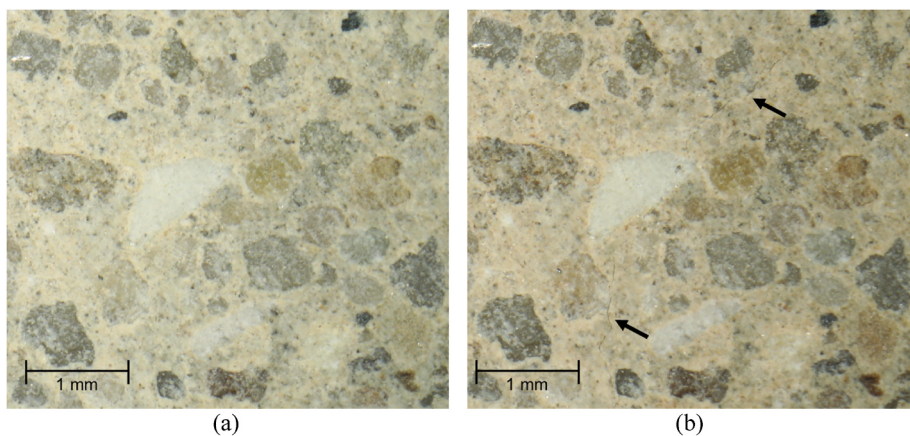


**Fig. 5.** Detailed surface photographs of the surface damage area 1: (a) before and (b) after fire damage. Microcracks are indicated by arrows.

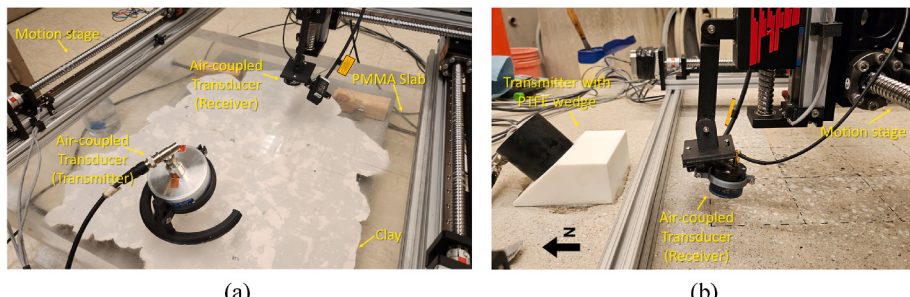


**Fig. 6.** Experimental setup: (a) Fully contactless Rayleigh wave scanning configuration for the PMMA slab and (b) semi-contactless Rayleigh wave scanning configuration for the concrete slab.

addition, as can be seen in Fig. 6 (a), clay was attached to the bottom surface of the slab to attenuate any wave reflection from the bottom surface to the top surface. A 4-cycle tone burst signal with a frequency of 49 kHz, modulated by Tukey window, was used as the excitation source with an excitation voltage of 140 V. The received time-domain signals using ACT were averaged 100 times with a DAQ system (PicoScope 5442B) to enhance the SNR. Signal data were collected every 5 mm at a sampling rate of 12.5 MS/s. For the spatial scanning a 2-D scanning frame was used, which is a ball-screw linear motion system with a position accuracy of  $\pm 0.02$  mm, as specified by the manufacturer (FUYU automation). Fig. 6 (b) shows the semi-contactless experimental setup used for the concrete slab. To generate Rayleigh waves, a contact transducer with a center frequency of 100 kHz (OLYMPUS V1011) was used, mounted on a wedge made of PTFE to generate the surface waves effectively. The angle of the wedge is  $40^\circ$ . Considering that the measured P-wave velocity of PTFE is 1316 m/s and typical concrete P-wave velocity is in the range between 3600–4300 m/s, the angle is slightly higher than the 2<sup>nd</sup> critical angle. This angle is intentional to encourage the Rayleigh wave and suppress P- and S-wave components; the angle is intentionally set slightly higher than the theoretical value. Two data sets were collected, one for the cold joint (soft inclusion) defect and another for the surface damage region. A tone burst signal with a frequency of 100 kHz, modulated by Tukey window, was used as excitation sources. For the cold joint defect, a 5-cycle excitation signal was used and for the surface damage regions a 16-cycle excitation signal was used. Differing excitation signals were intentionally used to explore if the measurement or PINN prediction results are dependent on the specific excitation signal. The received time-domain signals using ACT were averaged 100 times with a DAQ system to enhance the SNR. Signal data were collected every 5 mm for the cold joint defect region and every 4 mm for the surface damage region, at a sampling rate of 12.5 MS/s. The same motion 2-D scanning frame was used as before.

## 5. Results

### 5.1. PMMA slab

The experimental results of the PMMA slab measurements are presented in Fig. 7 (a), (b), and (c), which show the wavefield data in the 2-D spatial domain at different propagation times: 290, 315, and 340  $\mu$ s. Appendix A provides a detailed description of the procedure used to obtain the experimental wavefields from the measured data. The scanning area was about  $0.1 \times 0.1$  m. Coherent ballistic propagating wavefronts are evident and there is no noticeable scattering observed. The predicted surface wave velocity from a PINN model is shown in Fig. 8 (a). The model was trained to predict surface wave velocity: the model training data are the surface wavefield data and 70 % of the data corresponding to randomly selected spatial coordinates. However, to facilitate comparison with UPV data (considered as the true, verifiable value), the surface wave velocity prediction map was converted to a P-

wave velocity prediction map using

$$V_p = V \frac{1 + \nu}{0.87 + 1.12\nu} \sqrt{\frac{2(1 - \nu)}{1 - 2\nu}}. \quad (5)$$

This equation can be obtained from the approximate solution of the Rayleigh wave [48] ( $\eta = (0.87 + 1.12\nu)/(1 + \nu)$ ) and  $G = E/2(1 + \nu)$ , through algebraic manipulation. In this case, the Poisson's ratio was assumed to be 0.335, which falls within the typical expected range for PMMA. The resulting P-wave velocity prediction map, shown in Fig. 8 (b), exhibits relatively consistent values across the specimen, with minor variations. These disruptions are likely due to the interference of the Rayleigh wave with other wave modes, such as reflected P- or S-waves from the specimen's bottom surface. The mean value of the P-wave velocity prediction from the PINN model is 2746.8 m/s, with COV of 0.4 %. The prediction error for the P-wave velocity, relative to the reference value (shown in Table 2), is 0.34 % determined by the relative L<sup>2</sup> norm.

### 5.2. Concrete slab

Fig. 9 (a), (b), and (c) present the wavefield data of the concrete slab near the inclusion defect area in the 2-D spatial domain at different propagation times: 180, 220, 270  $\mu$ s. The scan area was  $0.22 \times 0.21$  m and the wavefield data were collected every 5 mm in both the x and y directions. Because of the subsequent casting of the inclusion part concrete specimen, the surface of the concrete slab was not even, causing lift-off distance (distance between ACT and the specimen surface) variation. To compensate for this, a laser displacement sensor was installed next to the receiver to measure the lift-off distance variation over space. After collecting the lift-off variation data, the wavefield data were compensated to account for this variation. Appendix B provides a detailed description of the lift-off distance variation compensation procedure. In the measurement results, coherent ballistic propagating wavefronts are clearly seen in Fig. 9 (a). Additionally, a moderate amount of wave scatter is observed at the boundaries of the cold joint or the inclusion area (at around  $x > 0.1$  and  $y < 0.1$ ), as indicated by the red arrows in Fig. 9 (b) and (c), which disrupts the ballistic wavefront. As before, 70 % of the total experimental measurement data were randomly selected to train the PINN models, with the remaining 30 % left unused. Fig. 10 (a) presents the PINN model's prediction of the surface wave velocity map. Notably, three distinct dark lines, representing areas of low velocity, correspond to the cracks shown in Fig. 11. The widths of the horizontal and vertical cracks are at the millimeter-scale, while the diagonal crack is at the micrometer-scale. Quadrants I, II, and III of Fig. 10 (a) correspond to areas with the Pristine material mixture, while quadrant IV corresponds to the area with the inclusion mixture. The P-wave velocity prediction map, shown in Fig. 10 (b), was obtained using Eq. (5). The area within the red dashed line, corresponding to the inclusion area, has a lower mean P-wave velocity of 3568 m/s. Conversely, the areas enclosed by the blue dashed or dotted lines, which correspond to the pristine areas, exhibit a mean P-wave

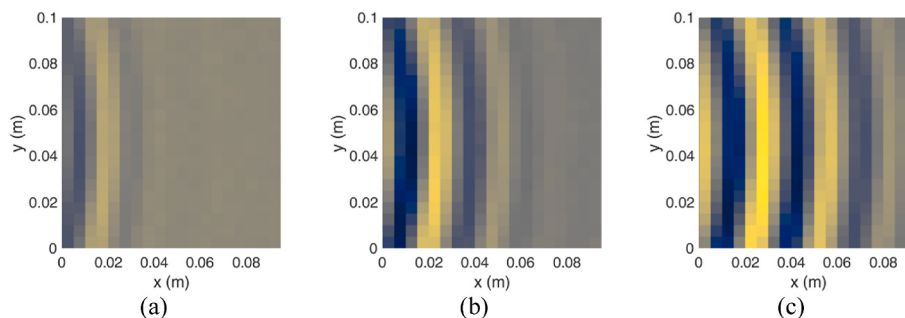


**Fig. 7.** Snapshots of surface wave propagation in the PMMA slab specimen at different propagation times: (a) snapshot at 290  $\mu$ s, (b) snapshot at 315  $\mu$ s, and (c) snapshot at 340  $\mu$ s.

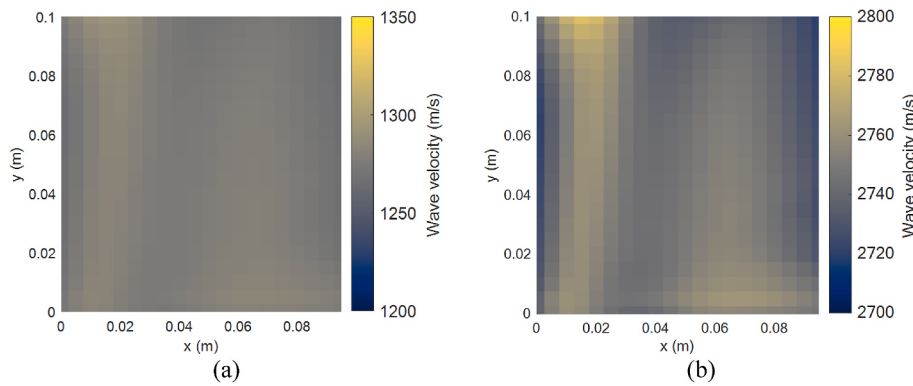


**Fig. 8.** PINN prediction results for the PMMA slab: (a) space-dependent surface wave velocity map and (b) P-wave velocity map.

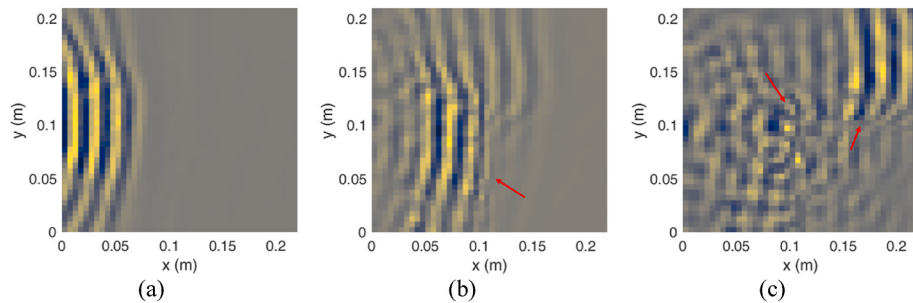


**Fig. 9.** Snapshots of experimental wave propagation in the large-scale concrete slab near the inclusion defect area at different propagation times: (a) snapshot at 180  $\mu\text{s}$ , (b) snapshot at 220  $\mu\text{s}$ , (c) snapshot at 270  $\mu\text{s}$ . The red arrows indicate wave scattering at the boundaries of the cold joints. (For interpretation of the references to color in this figure legend, the reader is referred to the Web version of this article.)

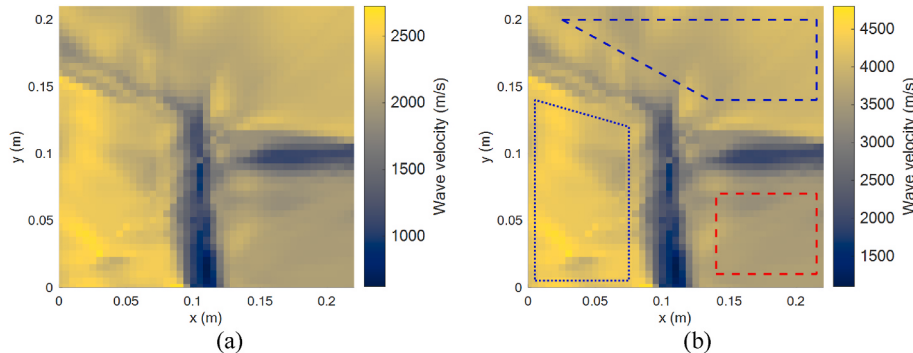


**Fig. 10.** PINN prediction results from the large-scale concrete slab around the inclusion defect area: (a) space-dependent surface wave velocity map and (b) converted P-wave velocity map. The area enclosed by blue lines represents the regions used to calculate the mean wave velocity for the pristine area, while the area within the red dashed line indicates the region used to calculate the mean wave velocity for the inclusion area. (For interpretation of the references to color in this figure legend, the reader is referred to the Web version of this article.)

velocity of 4081 m/s. The relative error of the predicted P-wave velocity results for the pristine area and the inclusion area are 1.0 % and 2.1 %, respectively, compared to the reference data.

Fig. 12 (a), (b), and (c) present the experimental wavefield data of the concrete slab specimen nearby the surface flame-damaged area captured at different propagation times: 150, 180, 210  $\mu\text{s}$ . The scan area measured  $0.18 \times 0.16 \text{ m}$ , with data collected every 4 mm in both the  $x$  and  $y$  directions. The early time snapshot reveals coherent ballistic propagating wavefronts with no other anomalies or disruptions seen. A slight delay in the wavefront is observed at about  $y = 75 \text{ mm}$ , seen in Fig. 12 (b), which becomes more pronounced in Fig. 12 (c). However, no significant wave scatter is observed. As in the previous cases, 70 % of the total measurement data were randomly selected to train the PINN models. Fig. 13 (a) presents the PINN model's prediction of the surface

wave velocity map. In the middle of the map there is a distinct dark area, representing areas of low velocity that corresponds to the surface damage area shown in Fig. 4(a) and (b). The P-wave velocity prediction map, shown in Fig. 13 (b), was obtained using Eq. (5). The area within the red dashed line, corresponding to the surface damage area, has a lower mean P-wave velocity of 3616 m/s. Conversely, the areas enclosed by the blue dashed lines (one positioned on the outskirts and the other centrally located), corresponding to the pristine area, have a mean P-wave velocity of 3932 m/s. In this case, it was not feasible to collect reference measurement data on the surface damage area due to the difficulty in replicating the exact extent of the damage in a companion specimen. Therefore, only the predicted damage area is discussed here and no direct comparison of wave velocity with reference data (e.g., UPV test) is made. As shown in Fig. 4 (a), the expected fire damage area

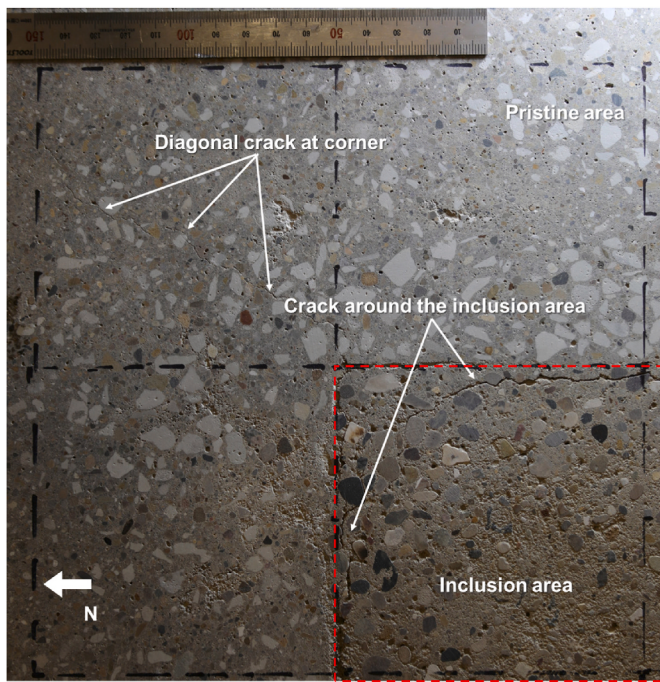


**Fig. 11.** Photograph of the large-scale concrete slab specimen surface nearby the inclusion area. The image shows millimeter-scale width cracks around the inclusion area and a micrometer-scale diagonal crack extending into the pristine area. The ruler in the image provides the millimeter scale reference.

is  $87 \times 40$  mm. The damage area predicted by the P-wave velocity map from the PINN model is  $88 \times 36$  mm. The model demonstrates a prediction error of 8.97 % in terms of defect area estimation.

## 6. Conclusions

This study demonstrates the effectiveness of using physics-informed neural networks (PINNs) to interpret ultrasonic scanning data to detect defects in concrete. PINN models were employed to predict space-dependent coefficients, specifically the wave velocity, of the governing wave equation using a subset of a simple time-domain wavefield data set. The performance of the proposed method was validated using experimental ultrasonic Rayleigh wave data collected from a PMMA slab and a large-scale concrete slab containing multiple defects including cold joints with cracks and surface fire damage. In all cases, the space-dependent wave velocity maps predicted by the PINN models enable material property characterization and defect detection. The defect detection was achieved by quantitative evaluation of local material properties, the wave velocity, rather than relying on a separate custom damage index. For the PMMA slab, the PINN model predicted P-wave velocities with an error of 0.34 % with respect to confirming measurements using the standard ultrasound pulse velocity (UPV) method. The large-scale concrete slab analysis highlighted the PINN model's ability to accurately locate defects by identifying the position and areal extant of inclusion defects and micrometer-scale cracks based on local P-wave velocity; velocity prediction errors of 1 % for pristine areas and 2.1 % for inclusion areas were obtained. The model predicted the extent of surface damage area with an error of 8.97 %. The PINN-predicted wave velocity map has a finer spatial resolution than that offered by other conventional ultrasonic imaging methods to the extent that the PINN results were able to detect sub-wavelength sized cracks. This ability to detect sub-wavelength features with ultrasonic waves is attributed to the physics-informed architecture, which incorporates wave propagation governing equations during training. Unlike conventional methods that analyze individual waveforms in isolation, PINN's holistic approach processes the entire spatio-temporal wavefield simultaneously, enabling the detection of subtle wave-damage interactions that would be

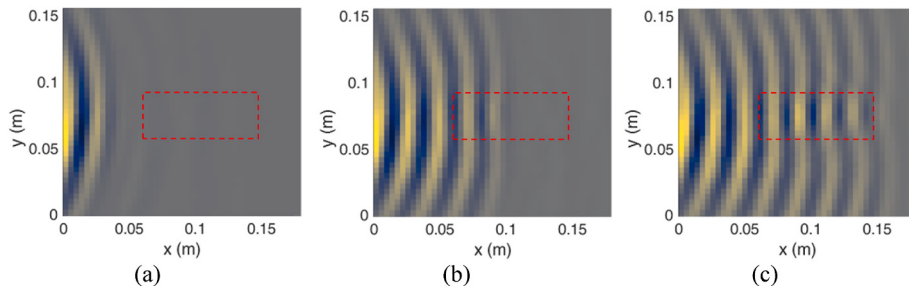


**Fig. 12.** Snapshots of experimental wave propagation from the large-scale concrete slab near the surface flame-damaged area (indicated by red dashed lines) at different propagation times: (a) snapshot at 150  $\mu$ s, (b) snapshot at 180  $\mu$ s, (c) snapshot at 210  $\mu$ s.

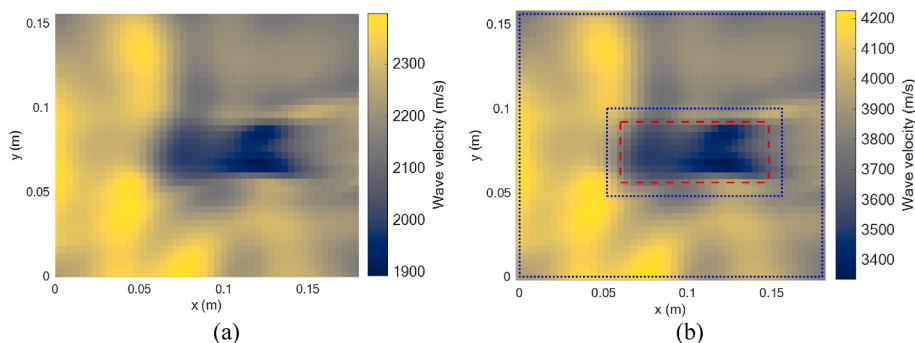


**Fig. 13.** PINN prediction results for the large-scale concrete slab near the surface damage area: (a) space-dependent surface wave velocity map and (b) converted P-wave velocity map. The area enclosed by the blue dotted lines represents the region used to calculate the mean wave velocity for the pristine area, while the area within the red line indicates the region used to calculate the mean wave velocity for the defect area. (For interpretation of the references to color in this figure legend, the reader is referred to the Web version of this article.)

undetectable through traditional analysis. This study builds on previous work exploring the potential of PINN applications for characterization of cementitious and heterogeneous materials using 1-D experimental and simulated data [51], as well as 2-D simulated data [52]. Our PINN approach offers several advantages over conventional ultrasonic imaging: (1) A well-trained PINN model can be used for super-resolution imaging [52]; (2) other material properties beyond wave velocity (such as dissipation [52]) can be predicted simultaneously if appropriate governing equations and appropriate physical bases are used; and (3) obtaining a similar map using the traditional pitch-catch method requires precise adjustment of wavefront and wave arrival time, which is labor-intensive. In contrast, the proposed method can achieve good results using simple wavefield measurement data without additional preprocessing. Future work should explore other geometries such as thin plates (Lamb waves), extraction of additional material characteristics such as dissipation/attenuation, and evaluate PINN performance with low signal-to-noise ratio signals and sparse data sets.

## Appendix A. wavefield reconstruction and training data

This appendix describes the snapshot reconstruction procedures and detailed explanation of training data used in the physics-informed neural networks. The manuscript presents wavefield data as two-dimensional spatial images (snapshots) at discrete time intervals, reconstructed from multiple time-domain signals, as illustrated in Fig. A-1. The scan area (top left) presents two representative data collection points: (0.05, 0.05) and (0.075, 0.1), marked by blue and red dots, respectively. Although only two points are shown here as examples, the data acquisition was carried out at regular spatial intervals of 4 or 5 mm, depending on the samples in the manuscript. The time-domain signals recorded at these coordinates are shown in the bottom panels of Fig. A-1. To reconstruct a snapshot image, the amplitude ( $u$ ) is extracted at a specific temporal point for each spatial coordinate. For instance, at  $t = 180 \mu\text{s}$ , the corresponding amplitudes (indicated by colored circles on the waveforms) are mapped to their respective spatial coordinates, resulting in points in the top right panel. This spatial-temporal mapping procedure is repeated for all measurement points across different time intervals to generate a comprehensive series of snapshot images, allowing the visualization of wave propagation throughout the scanned region.

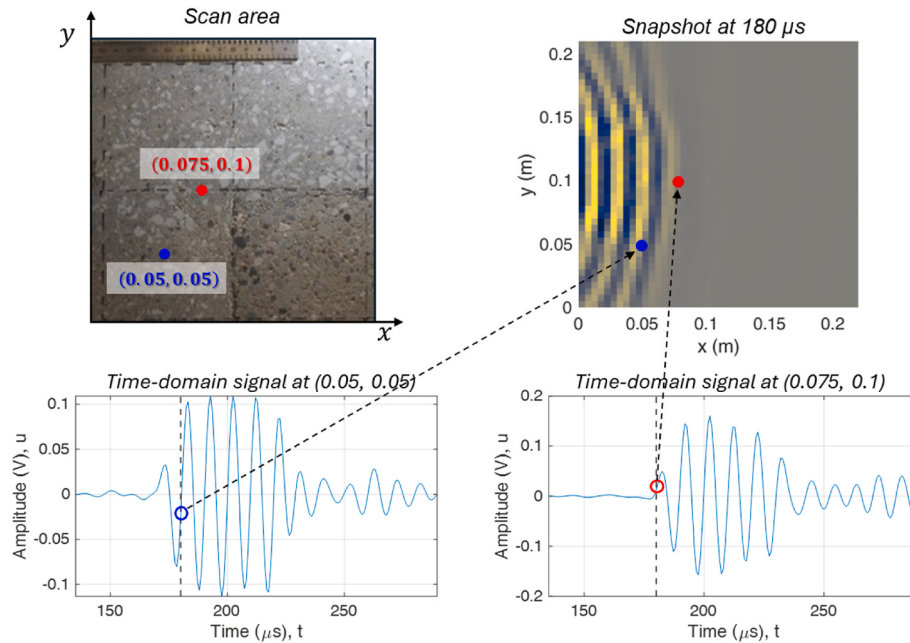


**Fig. A-1.** Illustration of the wavefield data reconstruction process. Top left: scan area showing two representative measurement coordinate points marked in blue and red, respectively. Top right: reconstructed wavefield snapshot at  $t = 180 \mu\text{s}$ . Bottom panels: time-domain signals recorded at the two measurement coordinate points.

The waveform data in Fig. A-1 represent the amplitude  $u(t)$  at specific spatial coordinates, which can be expressed as a function  $u(x,y,t)$ . For the illustrated measurement points, the data are denoted as  $u(0.05, 0.05, t)$  and  $u(0.075, 0.1, t)$ , where  $t$  ranges from 135 to 290  $\mu\text{s}$ . To systematically describe the training dataset structure, consider a scan area spanning  $x \in [10, 12] \text{ cm}$  and  $y \in [5, 10] \text{ cm}$ , with measurements taken at 1 cm intervals. Temporal data are collected from 0 to 0.9  $\mu\text{s}$  at 0.1  $\mu\text{s}$  intervals. This sampling method yields 180 total data points ( $3 \times 6 \times 10$ ), as shown in Figure A-2. The complete training dataset can be represented as  $\{[x_i, y_i, t_i, u_i]\}_{i=1}^{180}$  where  $[x_i, y_i, t_i]$  constitutes the input features and  $u_i$  represents the corresponding output values. As illustrated in Fig. A-2, columns 2–4 contain the input data, while column 5 contains the output data.

# of data		Input		output	
N	x	y	t	u	
1	10	5	0	0.21	
2	10	5	0.1	0.07	
⋮					
10	10	5	0.9	0.12	
11	10	6	0	0.01	
⋮					
61	11	5	0	0.58	
⋮					
180	12	10	0.9	0.18	

**Fig. A-2.** Structure of the training dataset organization. The table illustrates the format of input and output data, where N represents the data point index, x, y, and t are the input variables representing spatial coordinates and time, respectively, and u represents the output values.

## Appendix B. lift-off distance compensation

When using air-coupled transducers to measure mechanical wave propagation, the lift-off distance, or gap between the target surface and the air-coupled transducer (ACT), plays a critical role. The influence of lift-off distance variation is significant and may require a compensation because small changes in the lift-off distance can induce significant errors in the wave velocity measurement when using air-coupled sensors such as ACT or MEMS (Micro-Electro-Mechanical Systems). For example, consider a scenario where the wave velocity in the target sample is 4000 m/s, meaning that the wave takes 2.5  $\mu$ s to travel 10 mm in the sample. If two ACT measurements are taken 100 mm apart under constant lift-off distance conditions, the travel time in air cancels out, resulting in a successful estimate of the wave velocity at 4000 m/s. However, if the lift-off distance at the two measurement points increases by only 1 mm and the sound velocity in the air is 340 m/s, the wave arrival time at the later measurement point is delayed by 2.9  $\mu$ s due to the increased lift-off distance. Consequently, the estimated wave velocity drops to 1837.8 m/s, resulting in a significant error of 54 %.

Variations in lift-off distance are principally caused by two factors: undulation of the sample surface or vertical motion variation of the motion stage to which the ACT is attached. In both cases, attaching a laser displacement sensor to the motion stage can mitigate these problems, although it may not fully compensate for changes in wave behavior owing to geometric changes. With a laser displacement sensor, it is easy to construct a lift-off distance profile between the ACT and the sample. If the lift-off distance profile varies spatially, as illustrated in Fig. B-1 (a), then the time-domain signals of the wave propagation data collected using an ACT are also affected as illustrated in Fig. B-1 (b). This schematic illustrates the delay in wave arrival time (green) caused by an increase in lift-off distance in a homogeneous medium, with the three circular points indicating the positions of signal feature collected using ACT. Even if the material properties of the medium remain constant in space, the variation in lift-off can result in an apparent slower wave velocity prediction between the blue and green points and a faster wave velocity prediction between the green and red points. Fortunately, the lift-off distance measured by a laser displacement sensor can be easily converted to time using the speed of sound in the air, allowing the wave arrival time to be compensated as illustrated in Fig. B-1 (c).

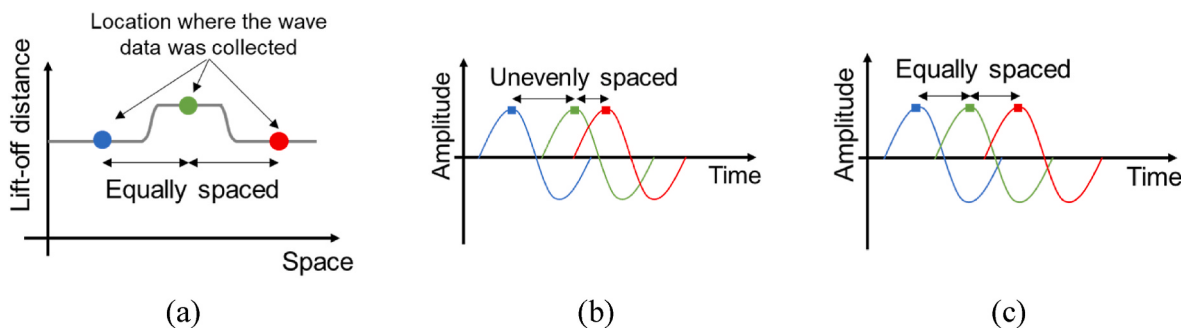


**Fig. B-1.** Illustration of lift-off distance variation compensation: (a) lift-off distance profile obtained using a laser displacement sensor, (b) time-domain signals affected by lift-off distance variation, and (c) compensated time-domain signals using the lift-off distance profile.

When using a laser displacement sensor to compensate for lift-off distance variation, the resolution of the sensor is important. The sampling interval ( $dt$ ) of the time domain signal is 80 ns when the sampling rate in a DAQ system is set to 12.5 MS/s. In this experimental configuration, lift-off distance variations greater than 27.2  $\mu$ m could be potentially affect the measurement results (when speed of sound is 340 m/s and sampling interval is 80 ns:  $340 \text{ m/s} \times 80 \text{ ns} = 27 \mu\text{m}$ ). The resolution of a laser displacement sensor, unless it is a low-end device, is found to be sufficient to detect such small displacements. For example, the optoNCDT 1320-100 (mid-range device) from Micro-Epsilon used in this research has linearity and repeatability cataloged at better than  $\pm 100 \mu\text{m}$  and 10  $\mu\text{m}$ , respectively. The calibration for this particular device further refines the linearity to better than  $\pm 20 \mu\text{m}$ . As a result, the variation in lift-off distance is expected to be effectively compensated by the laser-based lift-off data, ensuring the integrity of the noncontact sensing method.

In this study, the PMMA slab and the surface damage area on the large-scale concrete slab have a flat and even surface, so that the lift-off distance compensation was not required. However, the area around the inclusion defect area on the concrete slab is not totally flat and even. To compensate for this issue, a laser displacement sensor was installed next to the receiver to measure the lift-off distance variation over space as shown in Fig. B-2. Fig. B-2 (a) shows the raw data measured with a laser displacement sensor for the large-scale concrete slab near the inclusion defect area. Fig. B-2 (b) represents the data that has been refined by applying a Gaussian filter to mitigate measurement inaccuracies or other noises, and further normalized so that the minimum lift-off is zero. The filtered data are then converted to time data using the speed of sound (346 m/s, typical for room temperature conditions). The time data are then applied to the wavefield data to compensate for variations in the lift-off distance.

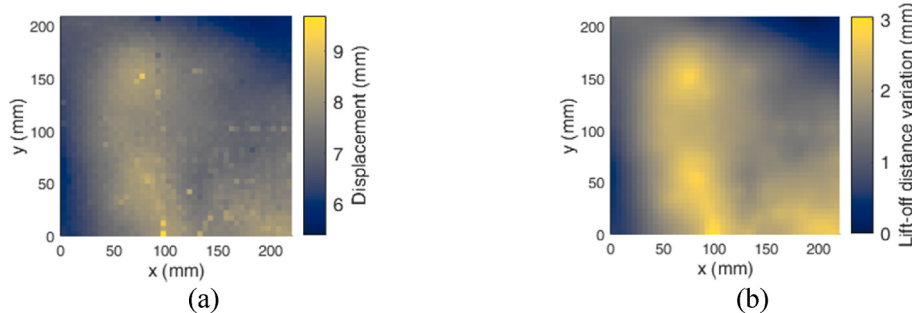


**Fig. B-2.** Variation in lift-off distance for the large-scale concrete slab near the inclusion defect area: (a) raw data illustrating the initial measurements, and (b) data after Gaussian filtering.

## Data availability

Data will be made available on request.

## References

- [1] 2021 Report card for America's infrastructure. Washington, DC: American Society of Civil Engineers; 2021.
- [2] Ji Y, Chen A, Chen Y, Han X, Li B, Gao Y, et al. A state-of-the-art review of concrete strength detection/monitoring methods: with special emphasis on PZT transducers. *Construct Build Mater* 2023;362:129742.
- [3] ACI Committee 228. In-Place methods to estimate concrete strength (ACI 228.1R-03). American Concrete Institute; 2003.
- [4] ACI Committee 228. Report on nondestructive test methods for evaluation of concrete in structures (ACI 228.2R-13). American Concrete Institute; 2013.
- [5] ASTM C803/C803M-18. Test method for penetration resistance of hardened concrete. West Conshohocken, Pennsylvania: ASTM International; 2018. [https://doi.org/10.1520/C0803\\_C0803M-18](https://doi.org/10.1520/C0803_C0803M-18).
- [6] ASTM C900-19. Test method for pullout strength of hardened concrete. West Conshohocken, Pennsylvania: ASTM International; 2019. <https://doi.org/10.1520/C900-19>.
- [7] ASTM C42/C42M-20. Test method for obtaining and testing drilled cores and sawed beams of concrete. West Conshohocken, Pennsylvania: ASTM International; 2020. [https://doi.org/10.1520/C0042\\_C0042M-20](https://doi.org/10.1520/C0042_C0042M-20).
- [8] ASTM C805/C805M-18. Test method for rebound number of hardened concrete. West Conshohocken, Pennsylvania: ASTM International; 2018. [https://doi.org/10.1520/C0805\\_C0805M-18](https://doi.org/10.1520/C0805_C0805M-18).
- [9] ASTM C1383-15. Test method for measuring the P-wave speed and the thickness of concrete plates using the impact-echo method. West Conshohocken, Pennsylvania: ASTM International; 2015. <https://doi.org/10.1520/C1383-15R22>.
- [10] ASTM C597-16. Test method for pulse velocity through concrete. West Conshohocken, Pennsylvania: ASTM International; 2016. <https://doi.org/10.1520/C0597-16>.
- [11] ASTM C1040/C1040M-16a. Test methods for in-place density of unhardened and hardened concrete, including roller compacted concrete, by nuclear methods. West Conshohocken, Pennsylvania: ASTM International; 2016. [https://doi.org/10.1520/C1040\\_C1040M-16A](https://doi.org/10.1520/C1040_C1040M-16A).
- [12] ASTM D4788-03. Test method for detecting delaminations in bridge decks using infrared thermography. West Conshohocken, Pennsylvania: ASTM International; 2022. <https://doi.org/10.1520/D4788-03R22>.
- [13] ASTM G57-20. Test method for field measurement of soil resistivity using the wenner four-electrode method. West Conshohocken, Pennsylvania: ASTM International; 2020. <https://doi.org/10.1520/G0057-20>.
- [14] Luukkala M, Heikkila P, Surakka J. Plate wave resonance — a contactless test method. *Ultrasonics* 1971;9:201–8. [https://doi.org/10.1016/0041-624X\(71\)90387-8](https://doi.org/10.1016/0041-624X(71)90387-8).
- [15] Chimenti DE. Review of air-coupled ultrasonic materials characterization. *Ultrasonics* 2014;54:1804–16. <https://doi.org/10.1016/j.ultras.2014.02.006>.
- [16] Deka M. Air-coupled ultrasonic transducer for NDE. IEEE 1987 ultrasonics symposium. 1987. p. 543–6. <https://doi.org/10.1109/ULTSYM.1987.199017>.
- [17] Grandia WA, Fortunko CM. NDE applications of air-coupled ultrasonic transducers. In: 1995 IEEE ultrasonics symposium. Proceedings. An international symposium, 1; 1995. p. 697–709. <https://doi.org/10.1109/ULTSYM.1995.495667>.
- [18] Essig W, Bernhardt Y, Döring D, Solodov I, Gautzsch T, Gaal M, et al. Air-coupled ultrasound—emerging NDT method. *ZfP-Zeitung* 2021;173:32–43.
- [19] Zhu J, Popovics J. Non-contact detection of surface waves in concrete using an air-coupled sensor. In: AIP conference proceedings, 615. Brunswick, Maine (USA): AIP; 2002. p. 1261–8. <https://doi.org/10.1063/1.1472940>.
- [20] Purnell P, Gaal TH, Hutchins DA, Berriman J. Noncontact ultrasonic diagnostics in concrete: a preliminary investigation. *Cement Concr Res* 2004;34:1185–8. <https://doi.org/10.1016/j.cemconres.2003.12.012>.
- [21] Oh T, Popovics JS, Ham S, Shin SW. Improved interpretation of vibration responses from concrete delamination defects using air-coupled impact resonance tests. *J Eng Mech* 2013;139:315–24.
- [22] Evani SK, Spalvier A, Popovics JS. Air-coupled ultrasonic assessment of concrete rail ties. *NDT E Int* 2021;123:102511.
- [23] Ham S, Song H, Oelze ML, Popovics JS. A contactless ultrasonic surface wave approach to characterize distributed cracking damage in concrete. *Ultrasonics* 2017;75:46–57. <https://doi.org/10.1016/j.ultras.2016.11.003>.
- [24] Song H, Popovics JS. Contactless ultrasonic wavefield imaging to visualize near-surface damage in concrete elements. *Appl Sci* 2019;9:3005. <https://doi.org/10.3390/app9153005>.
- [25] Ahn E, Shin M, Popovics JS. Air-coupled ultrasonic diffuse-wave techniques to evaluate distributed cracking damage in concrete. *Ultrasonics* 2022;125:106800.
- [26] Song H, Feldman SB, Popovics JS. In situ detection and characterization of alkali-silica reaction damage in concrete using contactless ultrasonic wavefield imaging. *Cement Concr Compos* 2022;133:104661.
- [27] Choi H, Song H, Tran QNV, Roesler JR, Popovics JS. Contactless system for continuous monitoring of early-age concrete properties. *Concr Int* 2016;38:7.
- [28] Fradkov AL. Early history of machine learning. *IFAC-PapersOnLine* 2020;53:1385–90. <https://doi.org/10.1016/j.ifacol.2020.12.1888>.
- [29] Hochreiter S, Schmidhuber J. Long short-term memory. *Neural Comput* 1997;9:1735–80.
- [30] LeCun Y, Boser B, Denker JS, Henderson D, Howard RE, Hubbard W, et al. Backpropagation applied to handwritten zip code recognition. *Neural Comput* 1989;1:541–51. <https://doi.org/10.1162/neco.1989.1.4.541>.
- [31] Cortes C, Vapnik V. Support-vector networks. *Mach Learn* 1995;20:273–97.
- [32] Campbell M, Hoane AJ, Hsu F. Deep blue. *Artif Intell* 2002;134:57–83. [https://doi.org/10.1016/S0004-3702\(01\)00129-1](https://doi.org/10.1016/S0004-3702(01)00129-1).
- [33] Krizhevsky A, Sutskever I, Hinton GE. ImageNet classification with deep convolutional neural networks. *Adv Neural Inf Process Syst* 2012;25.
- [34] Goodfellow I, Pouget-Abadie J, Mirza M, Xu B, Warde-Farley D, Ozair S, et al. Generative adversarial nets. *Adv Neural Inf Process Syst* 2014;27.
- [35] Raissi M, Perdikaris P, Karniadakis GE. Physics-informed neural networks: a deep learning framework for solving forward and inverse problems involving nonlinear partial differential equations. *J Comput Phys* 2019;378:686–707. <https://doi.org/10.1016/j.jcp.2018.10.045>.
- [36] Lagaris IE, Likas A, Fotiadis DI. Artificial neural networks for solving ordinary and partial differential equations. *IEEE Trans Neural Network* 1998;9:987–1000. <https://doi.org/10.1109/72.712178>.
- [37] Psichogios DC, Ungar LH. A hybrid neural network-first principles approach to process modeling. *AIChE J* 1992;38:1499–511. <https://doi.org/10.1002/aic.690381003>.
- [38] Huang L, Qin J, Zhou Y, Zhu F, Liu L, Shao L. Normalization techniques in training dnns: methodology, analysis and application. *IEEE Trans Pattern Anal Mach Intell* 2023;45:10173–96.
- [39] Cybenko G. Approximation by superpositions of a sigmoidal function. *Math Control, Signals, Syst* 1989;2:303–14.

- [40] Hornik K, Stinchcombe M, White H. Multilayer feedforward networks are universal approximators. *Neural Network* 1989;2:359–66.
- [41] Linnainmaa S. Taylor expansion of the accumulated rounding error. *BIT Numerical Mathematics* 1976;16:146–60.
- [42] Baydin AG, Pearlmutter BA, Radul AA, Siskind JM. Automatic differentiation in machine learning: a survey. *J Mach Learn Res* 2018;18:1–43.
- [43] Popovics JS, Abraham O. 20 - surface wave techniques for evaluation of concrete structures. In: Maierhofer C, Reinhardt H-W, Dobmann G, editors. Non-destructive evaluation of reinforced concrete structures, 2. Woodhead Publishing; 2010. p. 441–65. <https://doi.org/10.1533/9781845699604.2.441>.
- [44] ASTM C215-02. Test method for fundamental transverse, longitudinal, and torsional resonant frequencies of concrete specimens. West Conshohocken, Pennsylvania: ASTM International; 2002. <https://doi.org/10.1520/C0215-14>.
- [45] Anson M, Newman K. The effect of mix proportions and method of testing on Poisson's ratio for mortars and concretes. *Mag Concr Res* 1966;18:115–30.
- [46] Mindess S, Young JF, Darwin D. Concrete. Hoboken, New Jersey: Prentice Hall; 2003.
- [47] Kolluru SV, Popovics JS, Shah SP. Determining elastic properties of concrete using vibrational resonance frequencies of standard test cylinders. *Cem Concr Aggregates* 2000;22:81–9.
- [48] Viktorov IA. Rayleigh and Lamb waves : physical theory and applications. New York: Plenum Press; 1967.
- [49] Hong J, Kim R, Lee CH, Choi H. Evaluation of stiffening behavior of concrete based on contactless ultrasonic system and maturity method. *Construct Build Mater* 2020;262:120717. <https://doi.org/10.1016/j.conbuildmat.2020.120717>.
- [50] Hong J, Park J, Choi H. Evaluation of mechanical properties for setting of cementitious materials using air-coupled ultrasonics. *JKCI* 2022;34:51–9. <https://doi.org/10.4334/JKCI.2022.34.1.051>.
- [51] Lee S, Popovics JS. Applications of physics-informed neural networks for property characterization of complex materials. *RILEM Technical Letters* 2023;7:178–88. <https://doi.org/10.21809/rilemttechlett.2022.174>.
- [52] Lee S, Popovics JS. The potential for material property characterization using physics-informed neural networks and ultrasonic wave data. *Res Nondestr Eval* 2024;1–21. <https://doi.org/10.1080/09349847.2024.2350398>.